

# Vortex Wake Effect on a Generic Small UAV Wing-Body in Formation Flight

Joey J. Westermeyer\*

*The University of Alabama, Tuscaloosa, Alabama, 35487*

This experiment measured how aerodynamic forces change with changes in relative positioning between a lead and trail aircraft in formation flight. The models used were representative of small unmanned aerial systems, and the test was completed at a low Reynolds number of 63,000. Aerodynamic forces and moments were measured, and a maximum lift coefficient increase of 0.125 was experienced by the trailing model. It was found that the maximum lift and rolling moment both occurred at the location where the trail aircraft is 0.83 wingspans outboard of the lead aircraft, where the outside wingtips of both models are nearly aligned, but slightly overlapped, as viewed from behind. Trailing distance between the two models appeared to have no correlation with both lift and rolling moment coefficients. Conclusions were drawn as to the relative positional sensitivities of lift benefits for different dimensions and the implications of this research for future work on implementing formation flight for efficiency increases to real world applications.

## I. Nomenclature

$A$	=	reference area, $bc$
$b$	=	wingspan
$c$	=	chord
$C_D$	=	drag coefficient, $\frac{D}{qA}$
$C_L$	=	lift coefficient, $\frac{L}{qA}$
$C_{ll}$	=	roll coefficient, $\frac{L_{roll}}{qAb}$
$C_M$	=	pitch coefficient, $\frac{M}{qAc}$
$C_N$	=	yaw coefficient, $\frac{N}{qAb}$
$C_S$	=	sideforce coefficient, $\frac{S}{qA}$
$D$	=	drag force
$L$	=	lift force
$L_{roll}$	=	rolling moment
$M$	=	pitching moment
$N$	=	yawing moment
$N$	=	sample size
$P$	=	probability
$q$	=	dynamic pressure, $\frac{1}{2}\rho U^2$
$Re$	=	Reynolds number
$S$	=	side force
$s_x$	=	standard deviation
$s_{\bar{x}}$	=	standard deviation of the mean
$t_{v,P}$	=	student's t-value
$U$	=	freestream speed
$\bar{x}$	=	average variable value
$\mu$	=	dynamic viscosity
$\rho$	=	density

---

\*Undergraduate Student, AIAA Student Member

## II. Introduction

Since the inception of the heavier-than-air aircraft, engineers have worked to make aircraft more efficient. More efficient designs allow lighter aircraft and lower fuel burns, which translate directly into reduced cost, increased profits, and reduced emissions for identical missions. Accordingly, many leaps in efficiency have been made over the course of aerospace history, and many advanced concepts for the future of aerial transportation are currently under study by NASA and industry partners [6].

One such idea is that of formation flight. Formation flight for human-made aircraft has historically been for non-aerodynamic purposes; military formations concentrate firepower and allow team tactics, civil formation flight improves air traffic control efficiency, and airshow formations showcase piloting skill. It has been proven that birds flying in formation experience efficiency benefits - one study measured geese heart rates are 16% lower when flying in formation than alone - but this has not been practically employed in man-made aircraft [12]. However, recent research on formation flight has attracted industry attention for its potential to reduce drag in cruise, with one NASA study finding up to 8% fuel savings for two Gulfstream G-IIIs in formation flight [7]. Experimental studies have also been performed to assess the fuel savings available from formation flight by NASA, DARPA, Airbus, Boeing, AFRL, and more [11].

However, few studies have examined on this concept for small unmanned aerial systems (sUAS's). These aircraft operate at much lower Reynolds numbers ( $< 200,000$ ) and tend to have smaller aspect ratios, which could effect the creation and interaction of the lead aircraft's wake with the trailing aircraft. Moreover, little research has been published that analyzes trailing distance's impact on the aerodynamic interactions in formation flight; the studies reference above published the fuel savings of different lateral and vertical locations at constant trailing distance [7]. As such, this study aims to quantify the aerodynamic interactions of a lead aircraft on a trailing aircraft with changes in relative location in all three dimensions. The results could be used to define optimal areas for trailing sUAS's to fly relative to lead sUAS's in formation, as well as how sensitive aerodynamic benefits are to errors in tracking that optimal location. This would ultimately increase efficiency of sUAS's, yielding increased range and reduced energy consumption. To this end, the aerodynamic effects of formation flight on generic sUAS wing-body models with a 15.5 cm (6 inch) wingspan. Forces and moments on a trail aircraft following a lead aircraft mounted at an angle of attack were measured for lateral separations of 0 to 4 wingspans, vertical separations from 0 to -0.66 wingspans, and axial/trailing separations from 1 to 6 wingspans.

## III. Relevant Theory

### A. Finite Wing Vortex Generation

When an aircraft generates lift, high pressure is generated beneath the wing and low pressure above. The pressure differences drives the air around the wingtip, forming a vortex at each wingtip of a finite wing. The resulting tip vortex causes induced drag, as well as upwash outboard of the wingtip that can be harnessed via formation flight [1]. This vortex can be modeled by Prandtl's lifting line theory. In this theory, the vortex system generated by a finite wing is modeled as a series of vortex "horseshoes" consisting of a bound vortex filament along the lifting line of the wing and free trailing vortex filaments that extend from the ends of the bound vortex rearwards [1]. The wake profile derived using this theory for a rectangular lift distribution is shown in Fig. 1.

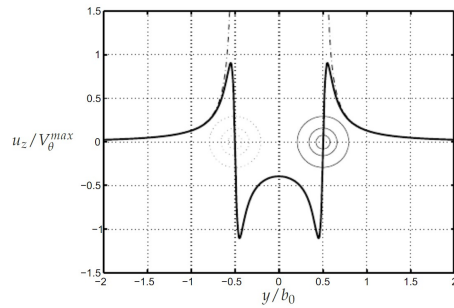


**Fig. 1 Finite Wing Wake Vertical Velocity Profile [3]**

As can be seen, a region of upwash exists outboard of each wingtip beyond at  $0.5y/b_0$ , where  $b_0$  is the wingspan for

Fig. 1. The concept of using formation flight stems from the existence of this upwash; flying an aircraft in upwash effectively rotates the lift and drag vectors of the wing forward relative to the reference frame of the aircraft, resulting in a net decrease in drag in the aircraft's reference frame [4]. An alternative way of viewing this is the updraft provides lift from its upward movement that the aircraft does not have to create, thus reducing the drag of the aircraft from lift creation.

The conclusion from this theory is that, for maximum drag reduction, the trailing aircraft should fly in the area of strongest updrafts created by the leading aircraft's wake. A theoretical calculation of these updraft velocities 4000 ft behind a Gulfstream G-III aircraft calculated by NASA is shown in Fig. 2. As can be seen from both Fig. 2 and Fig. 1, the strongest updraft occurs immediately outboard of the lead aircraft's wingtip projected along the flight path to the trailing aircraft's location, with corrections for the descent of the vortex wake and wind drift shown in Fig. 2 (black dot, cross track = 40 ft, vertical position = 0).

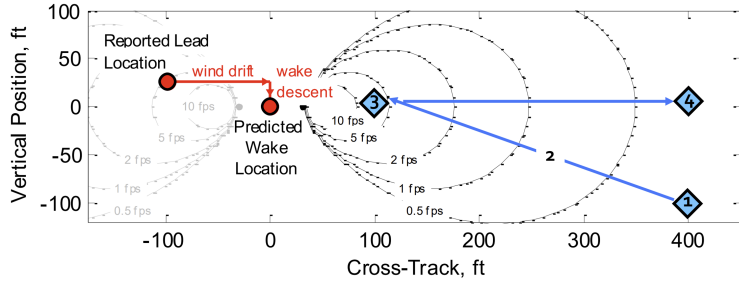


**Fig. 2 Predicted Upwash of Gulfstream G-III 4000 ft In Trail (Wingspan = 80 ft) [7]**

The effect of flying in this updraft, in real world operations, is the reduction in pitch angle (angle relative to Earth) of the trail aircraft to maintain the same angle of attack (angle relative to freestream) to create the same lift required for level flight. This has the aforementioned effect of rotating the lift and drag vectors forward, reducing drag and fuel consumption. However, if the pitch angle remains unchanged, a change in angle of attack will occur, and thus the lift of the trailing aircraft will increase due to the updraft. It is this lift increase that this experiment aims to measure, as explained in the following sections.

#### IV. Experimental Method

To perform this experiment, representative models of both lead and trail sUAS's were designed, manufactured, and mounted in the wind tunnel with three degrees of freedom. The testing procedure was designed such that data of sufficient quality and quantity was recorded from which to draw conclusions. The approaches to these requirements are detailed in the following sections.

##### A. Models

To design the models to be manufacturable, representative of a typical sUAS, and conducive to a successful experiment, many competing variables were taken into account: Reynolds number, load cell resolution, wind tunnel size, flow speed limitations, etc. To balance these requirements, the model size was chosen to have a 15.2 cm wingspan and body length, 3.8 cm chord, and 2.6 cm body diameter. This geometry results in an aspect ratio of 4, which is representative of many sUAS. The 15.2 cm wingspan allowed a lateral traverse of 4 wingspans with 1 wingspan of separation from the tunnel walls to avoid interference effects, which allows the trailing aircraft to traverse outside the majority of the lead's wake effects as shown in Fig. 2. Moreover, the resultant wing area, when combined with the Finner-Bryan wind tunnel's limiting operating speed of 25 m/s, would produce a calculated force of 0.217 N with a coefficient of lift of 0.1: a force well above the ATI-nano17 load cell's worst-case resolution of 0.0125 N [2]. Finally, the total frontal area of both models is less than 1% of the wind tunnel's cross section. This value is far below the 5% blockage ratio below which results are normally unaffected by blockage [5][13].

The models were designed in OpenVSP to determine the wing and vertical stabilizer locations and incidences. The final design of the identical lead and trail aircraft, as well as a sample aerodynamic analysis run in AEROVSP, is shown in Fig. 3. The models were designed for trimmed flight at an angle of attack of nine degrees with a calculated coefficient

of lift of 0.6 and a center of gravity placed at the airfoil quarter-chord. Furthermore, the models were designed such that they were statically stable with a static margin of 0.1. These are all parameters representative of conventionally-designed sUAS's in cruise conditions.

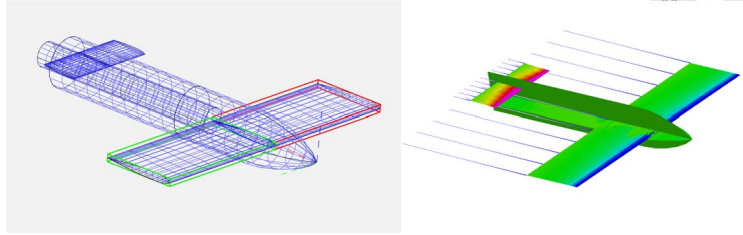


**Fig. 3 OpenVSP Model Design and Aerodynamic Analysis**

The fuselage design was 3D printed to obtain the desired fuselage shape, airfoil incidence angles, and mounting fixtures for use in this experiment. The airfoils were sheared from aluminum plating, resulting in flat plate airfoils for simplicity of manufacturing and aerodynamic analysis. The trailing aircraft was mounted at zero degrees angle of attack on a rear-mount sting attached to an ATI-nano17 6 degree of freedom load cell (Fig. 4), and the lead aircraft was mounted at the trim angle of attack of nine degrees on a vertical strut through the airfoil quarter-chord. Both aircraft were mounted slightly greater than two wingspans from both the floor and ceiling of the wind tunnel to avoid ground effects, 95% of which are absent beyond 1 wingspan of height above the ground [9].

The trailing aircraft sting attached to manually-adjustable vertical post, which mounted on a Velmex Traverse that electromechanically traversed the model laterally. The lead aircraft strut was mounted on a rail aligned with the freestream direction such that it could be manually moved to adjust the trailing separation of the two aircraft. This mounting scheme, along with arrows representing degrees of freedom in the mounts, is shown in Fig. 5. The blue arrow represents a movement direction controlled electromechanically via the Velmex Traverse, and the orange arrows represent manually adjusted movement directions.



**Fig. 4 Fully Built Trail Aircraft Model Mounted on Rear Sting and Load Cell**



**Fig. 5 Lead and Trail Aircraft Models Mounted in Wind Tunnel**

## B. Test Procedure

Aerodynamic force data was collected for points spanning a 3D space of relative trailing positions. To capture this large quantity of data efficiently and robustly, a custom virtual instrument (VI) script was written in LabVIEW to both record load cell data and drive the Velmex traverse. The LabVIEW program interfaced with the ATI-nano17 load cell via an SCXI strain gauge module with 1314 breakout, and interfaced with the Velmex traverse directly. Additionally, the tunnel was fitted with pitot-static probes upstream and downstream of the test section connected to a PSI-9016 pressure scanner. These measured the stagnation and static pressure of the flow, which were used to calculate the flow velocity. A Druck digital barometer was used to record the ambient pressure, and an Omega thermometer logger was used to record the ambient temperature.

During the experiment, the manually-adjusted dimensions were set, the tunnel was set to a speed of 25 m/s, and a lateral sweep of data was recorded by running the LabVIEW program. This was done for all test points in Table 1. Each vertical and axial separation distance were set manually on the trailing and lead aircraft, respectively (Fig. 5). Conversely, the LabVIEW program laterally traversed the trailing model automatically in 2.64 cm (1 inch) intervals for 24 intervals, recording 10,000 test points at 1000 Hz at each lateral location. This large sample size and frequency was chosen to reduce precision errors and capture any periodic or irregular forces arising from the vortex system of the lead aircraft. It should also be noted that the floor of the test section was not horizontal and aligned with the freestream, and thus the vertical distance of the trail aircraft was adjusted as the lead aircraft was moved forward in the freestream direction.

**Table 1 Test Matrix**

Variable	Test Points, Wingspans
Trailing distance	1, 1.6, 3, 6
Vertical Separation	0, -1/8, -1/4, -1/2, -3/4
Lateral Separation	0-4; 1/6 increments

Following data collection, MATLAB was used to nondimensionalize, synthesize, and visualize all data obtained during the tests. The definitions for force and moment coefficients were used to nondimensionalize these values, all position values were nondimensionalized according to the wingspan of the models, and the precision uncertainty values were calculated and plotted for all the data. The equations below were used for precision uncertainty calculations, where Eq. 1 relates a sample's standard deviation to its standard deviation of the mean. Eq. 2 was then used to calculate the uncertainty of each data point's average within a 95 % probability. This equation does, however, exclude bias errors that can arise from experimental design, instrumentation, or interference errors [8].

$$s_{\bar{x}} = \frac{s_x}{\sqrt{N}} \quad (1)$$

$$\bar{x} = \bar{x} \pm t_{v,P} s_{\bar{x}} \quad (2)$$

## C. Flow Visualization

Following the measurement of aerodynamic forces, the wake of the lead aircraft was visualized to track the wingtip vortex growth and core location. This was tested in the University of Alabama's Boundary Layer Wind Tunnel with a TSI BG-1000 bubble seeder and a Litron Nano TRL 425-10 2500 watt laser. The lead model was mounted at the beginning of the test section at the same nine degree trim angle of attack used in the force measurements, and the laser was formed into a sheet such that it would illuminate a lateral-vertical cross section of the test section behind the aircraft. The bubble seeder was allowed to fill the tunnel intake, the wind tunnel was activated and stabilized at 5 m/s, and a Nikon D300S camera was used to capture photos of the seeding illuminated by the laser sheet to visualize the wake flow field. This was repeated five times with the laser sheet placed to illuminate cross sections at trailing distances of 1, 2, 3, 5, and 8 wingspans behind the model. The 5 m/s speed for this test was chosen in contrast to the 25 m/s speed of the aerodynamic force tests to allow visualization of the flow; higher speeds resulted in dissipation and critically low density of the seeding such that the flow could not be adequately visualized. This test speed results in a Reynolds number of 12,600. While this is one fifth of the other test's Reynolds number of 63,000, both are well below the flat plate boundary layer transition Reynolds number regime of 150,000 to 1,500,000 [10].

To measure the location of the vortex core, photos were taken of an engineering scale placed at the same distance from the Nikon camera as the laser sheet in the experiments. These photos were superimposed on the flow visualization photos in Photoshop, the pixel distance between scale inch markers was used to calibrate Photoshop's ruler tool, which was then used to measure the location of the vortex cores, as estimated visually. This estimation was done by locating the absence of seeding at the vortex core, if it existed, or by finding the center of a circle drawn around the visible vortex structure, as shown in Fig. 6. The uncertainty of these locations was also estimated manually and later plotted with the vortex locations on the aerodynamic force contours with error bars.

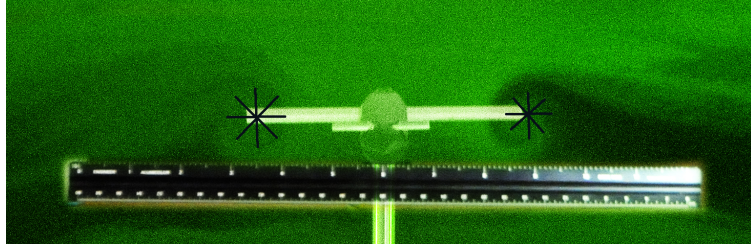


**Fig. 6 Vortex Core Location Measurement (ruler and circle centering superimposed)**

## V. Results and Discussion

### A. Representative Test Case

Before the data from all lateral sweeps is synthesized to create contours, a discussion of representative data from a single lateral sweep is necessary. Plots depicting force and moment coefficients for a representative lateral sweep at constant vertical and axial separation are shown in Fig. 7 and Fig. 9. As will be seen in later results, nearly all lateral sweeps agree with trends from this representative test case. The lateral position shown is the displacement of the trail aircraft's fuselage center from the lead's fuselage center, as shown in the left of Fig. 7. It should be noted that the depiction in the left of Fig. 7 shows a nonzero vertical displacement, while the data shown in Fig. 7 was a lateral sweep at a vertical displacement of zero.

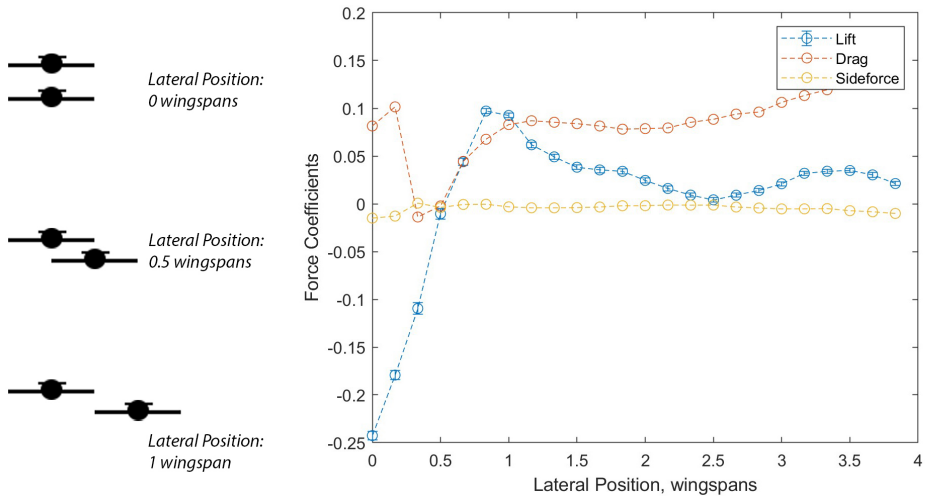


**Fig. 7 Representative Test Case Force Coefficients: lateral sweep at 1.5 wingspan trailing distance and 0 vertical displacement**

Firstly, as can be seen in Fig. 7, the sideforce is nearly zero throughout the lateral traverse, as expected. Also as expected, the lift of the trail aircraft begins at a minimum, where it is strongly negative, directly behind the lead aircraft

and its downwash, as shown in Fig. 1. Lift increases to a maximum at a lateral location of 0.83 wingspans, signifying the location where the trailing aircraft lifting surface is approximately entirely in upwash of the lead. Lift then decreases to zero, as is expected for the trail model mounted at an angle of attack of zero, as the model is further traversed laterally outside the lead's wake vortex system.

Of interest beyond this point is the lift increase of the trailing aircraft around 3.5 wingspans of lateral separation. This is not explained by Prandtl's lifting line theory, and is very consistent across the test cases. Tests done with no lead aircraft in the wind tunnel replicated the unexplained lift at 3.5 wingspans, despite measuring no lift in all other locations as expected. This suggests the unexpected lift is a result of some change in the flow field in this area of the test section and not an interaction with the lead aircraft. Accordingly, this research's discussion focuses on effects inboard of three wingspans lateral separation.

Secondly, the drag data in Fig. 7 disagrees with AEROVSP's calculation that the majority of drag experienced by the model is parasitic drag, and thus small lift changes will not appreciably increase total drag. Moreover, the drag measured by the load cell appeared to mirror small changes in sideforce, as shown in Fig. 8. Unit weight tests on the isolated load cell confirmed that sideforce was experimentally coupled to drag measurements, and thus this discussion does not examine drag data. Despite this, all other measurements were very repeatable, agreed well with theory, and agreed across test cases, and thus all other values were considered valid and are used in this discussion.

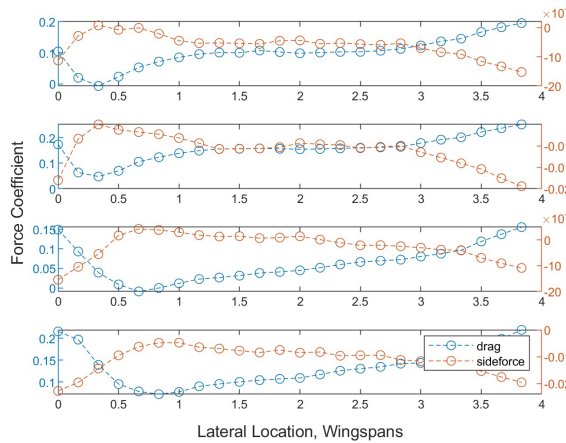


**Fig. 8 Representative Test Case Drag and Sideforce Coefficients**

Finally, the moment coefficients from the representative test case are shown in Fig. 9. While the yaw and pitching moments are simply reproductions of sideforce and lift due to the load cell's location at the rear of the aircraft, their agreement with the sideforce and lift plots in Fig. 7 validates those measurements, further lending credibility to the data and the following conclusions.

As expected, the rolling moment of the trail aircraft in Fig. 9 is zero directly behind the lead aircraft, where it experiences a symmetrical downwash in the wake of the lead aircraft (Fig. 1). Also as expected, the trailing aircraft experiences a negative (leftward) rolling moment when its wing is largely overlapped with the lead's wing. Here, right and left sections of the trail's wing experience contrasting upwash and downwash created right and left of the lead aircraft's wingtip, respectively (Fig. 1). Similarly, the rolling moment is positive (rightwards) when the trailing aircraft's wing is mostly in the upwash outboard of the lead's wingtip. In this location, the gradient of the lead's wake's upwash strength (Fig. 1) generates greater lift on the left of the trail's wing than the right, thus creating a rightward rolling moment. Lastly, the nonzero rolling moments with no apparent trend outboard of 1.5 wingspans are similar to the lift data in that they disagree with established theory, were repeated in tests with no lead aircraft, and will not be considered further in this discussion.

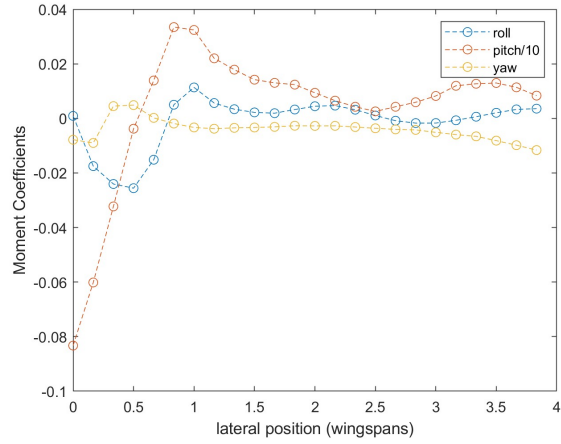


**Fig. 9 Representative Test Case Moment Coefficients: : lateral sweep at 1.5 wingspan trailing distance and 0 vertical displacement**

The uncertainty was calculated and plotted for all variables measured, but was so low due to the large, 10,000-measurement sample size at each point that the uncertainty error bars cannot be discerned on these plots. For example, the largest uncertainty in the lift coefficient was 0.003 at a lift coefficient of 0.1, corresponding to an uncertainty error of three percent. This uncertainty cannot be seen on these plots and thus was omitted.

## B. Contour Plots

Once all the data was processed and validated as in section V.A above, the data for all positions was synthesized into contour plots showing lift and rolling moment coefficient values in a cross section of the test section (Fig. 10 and Fig. 13). Both figures show contours for lateral-vertical cross sections at each of the four trailing distances where data was recorded according to Table 1. Dots were plotted along the contour plots to show points where data was sampled, and the top left corner of each contour plot is where the lead aircraft's fuselage center was located. Finally, the location 0.5 wingspans to the right of the photographed vortex location was plotted for each trailing distance with uncertainty error bars. This locations corresponds to where the left wingtip of the trailing aircraft is aligned with the vortex core, as interpolated from the flow visualization photos. An example of one of these photos is shown in Fig. 11.

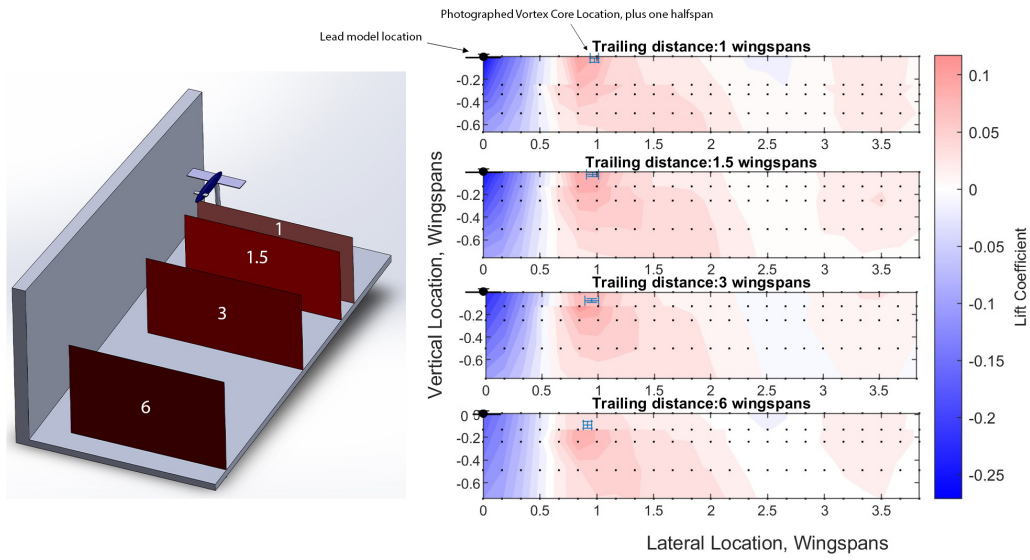


**Fig. 10 Cross-Sectional Lift Coefficient Contours**

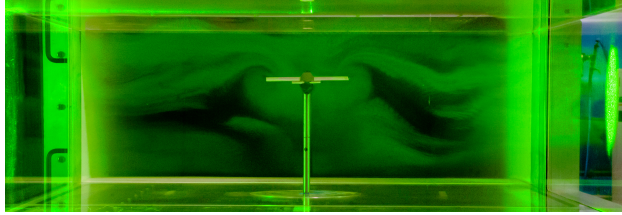


**Fig. 11 Flow Visualization Example Photo**

As can be seen in Fig. 10, the lift coefficient of the trail aircraft largely follows what is predicted by theory [4],[7], [3]. The trail aircraft consistently sees minimum lift directly behind the lead aircraft, maximum lift at 0.83 wingspans where the trail aircraft wing is in the upwash outboard of the lead's wingtip, and zero lift outside the influence of the lead's wake (Fig. 1). Also in alignment with theory is the descent of the maximum lift location with trailing distance, as the vortex system of the lead aircraft will descend as it travels farther behind the lead [4]. Finally, the measured lift increase corresponds with the vortex locations measured with flow visualization; both the descent of the vortex cores and the contraction of the vortices from the lead's wingtips agree with the location of maximum lift below and slightly inboard of the lead's wingtip (Fig. 10). The differences between the vortex core locations and the maximum lift locations could be explained by the different Reynolds numbers and wind tunnels used in aerodynamic force measurement and flow visualization, but the trends between the two experiments agree and correlate well with each other.

Another way to visualize the data shown in Fig. 10 is shown below in Fig. 12, which plots the lateral sweep of data that contains the maximum lift coefficient for each trailing distance. The result of this is a contour that can be viewed as a slice of the axial-lateral plane, but slightly declined to follow the descent of the lead aircraft's vortex system. Of great interest in Fig. 12 is the conclusion that lift benefits are relatively insensitive to changes in trailing distance at the separations tested. In fact, the maximum lift coefficient of 0.125 occurred at a trailing distance of 3 wingspans: the second largest tested.

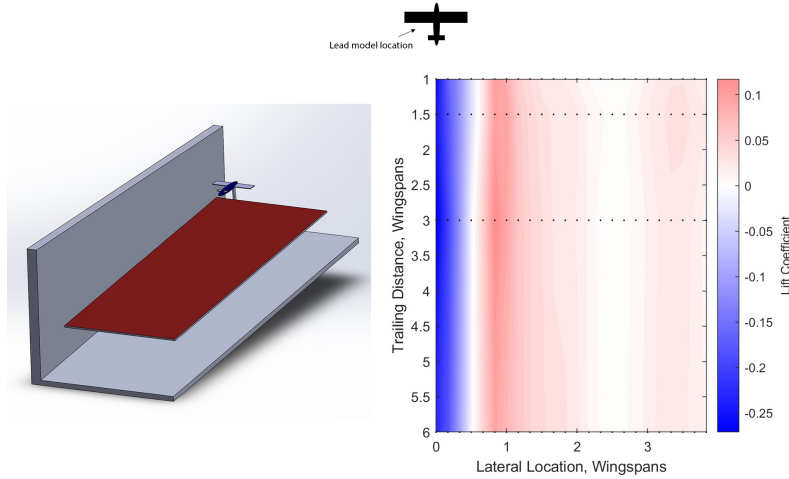


**Fig. 12 Lift Coefficient Plot for Trailing Distance vs. Lateral Location at Vertical Height with Maximum Lift**

Also of interest is Fig. 13, which is the roll moment coefficient corollary to Fig. 10. As expected from the representative test case analysis, the rolling moment coefficient is negative inboard of the lead aircraft wingtip – when the left and right wings of the trail aircraft experience downwash and upwash, respectively – and positive when the trail is entirely outboard of the lead's wingtip and roll is caused only by changes in the upwash strength across the trail aircraft's wingspan. As with the lift increase near the right wall of the test section, the unexplained subsequent increase of roll moment coefficient near 2 wingspans of lateral separation is shown to be very consistent across test cases regardless of lead aircraft position, potentially suggesting a flow field irregularity.

However, of greater interest to these conclusions is the comparison of Fig. 13 to its lift corollary in Fig. 10. As can be seen, the maximum lift location coincides nearly perfectly with that of the maximum roll moment location;

both occur between 0.83 and 1 wingspan of lateral separation for all test cases, and both descend vertically as trailing distance increases. This agrees with theory; the strongest upwash will produce both the largest lift benefit and the largest roll moment [4], [7]. This could be viewed both as a challenge and an opportunity. Flying in formation for efficiency benefits requires counteracting this rolling moment and encountering potential turbulence caused by the vortex, but conversely this coincidence of the location of maximum roll moment with that of maximum lift could be used to guide pilots and flight controllers to the area of maximum lift.

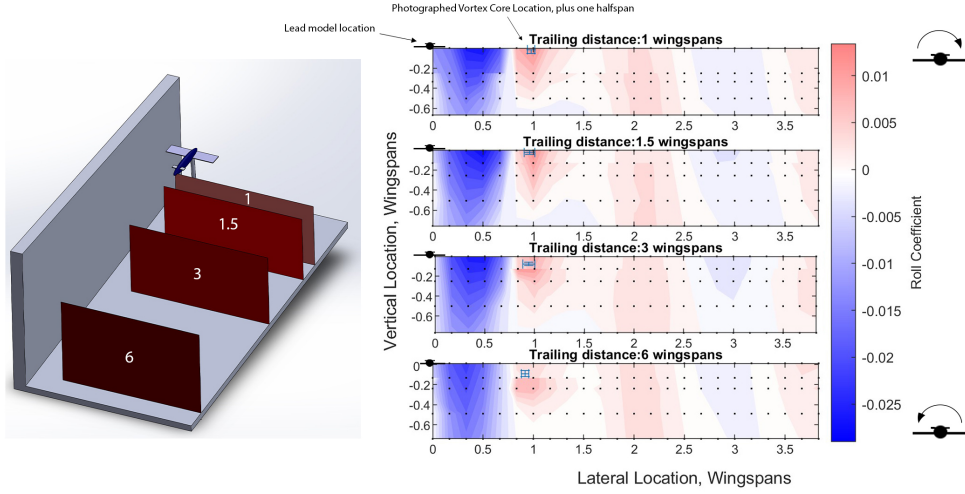


**Fig. 13 Cross-Sectional Roll Coefficient Contours**

## VI. Conclusions

This experiment tested small wing-body models representative of sUAS's to measure changes in aerodynamic forces with changes in relative positioning in formation flight. Tests varied positions in three dimensions at an average Reynolds number of 63,000 in the University of Alabama's Finnel-Bryan wind tunnel. While the drag data was found to be misleading, all other data inboard of two wingspans of lateral separation was repeatable, agreed well with theory, and allowed the following conclusions.

As expected, the maximum lift coefficient of 0.125 of the trail aircraft occurred when the trail and lead aircraft's outer wingtips were nearly aligned (lateral displacement of 0.83 wingspans), but displaced vertically to align with the descending wake of the lead. Also in this position was the maximum positive rolling moment measured in the experiment, which was in the direction of rolling the trail aircraft out and away from the lead. This location corresponds to the entire wing of the trail aircraft being in the strongest upwash generated by the lead's lifting surface, according to Prandtl lifting line theory.

Of interesting note from this experiment are the conclusions surrounding location sensitivity of lift benefits in formation flight. It was found that lift benefits are highly sensitive to changes in lateral and vertical position; positional inaccuracies of just one half wingspan from the optimum location could eliminate, or even invert, lift benefits. However, it was found that lift benefits are insensitive to changes in trailing distance, although theory suggests the dissipation of the lead's vortex system should decay lift benefits as trailing distance increases [4]. However, the results of this experiment do not show this, suggesting the time scale of this dissipation must be much larger than the time it takes the vortex to travel six wingspans aft of the lead at this experiment's speeds ( $\frac{36in}{25m/s} = 0.036$  seconds). This conclusion is of interest when implementing formation flight for efficiency increases, since the vertical and lateral positioning of aircraft are controlled directly by flight control surfaces and thus have relatively fast responses. In contrast, precise axial positioning of aircraft is difficult since this is indirectly controlled by flight speed, which has a much slower response time in aircraft. This meshes well with the relative dimensional sensitivities of lift benefits in formation flight; the dimensions that are more important for realizing lift benefits correspond to finer control authority in aircraft.

Also of interesting note from this experiment is the relation between maximum roll moment and maximum lift coefficient; they occur at the same location. This could be used in guiding both pilots and digital flight controllers to find the position for maximum lift benefits while in formation flight more accurately than other methods allow. This

is because obtaining precise relative positioning of two aircraft in real time, then acting on that position data, can be very difficult. GPS can be highly accurate, but has an associated lag time. Radar or Lidar systems that could precisely measure relative positioning could provide less lag time, but would be expensive and heavy to implement or retrofit. And, beyond these limitations, both of these position-based methods for formation flight have no ability to take vortex drift due to wind into account in finding the optimum formation flight position without some form of external wind sensor, which is another source of error and difficulty in measurement. The results of this experiment suggest that, if the ride quality were acceptable and the trail aircraft could handle the imposed loads, the trail aircraft could use the rolling moment, and thus the required aileron input required to counteract the rolling moment, to find the area of maximum lift benefit. This is promising because measuring aileron roll input required to maintain level flight could be instantaneous, while a lift benefit resulting in a drag reduction is usually measured with fuel flow, and thus lags significantly behind real-time aircraft behavior. Thus, rolling moment, which is a real-time indication, could be used to position a trail aircraft in the optimum position for lift benefits in formation flight.

## VII. Acknowledgments

The author thanks Dr. Paul Hubner for his guidance in the design, execution, and presentation of this experiment, as well as access to the University of Alabama's experimental aerodynamics equipment and knowledge base. The author also thanks Chris Jarmon and Andrew Bonacci for their guidance and participation in the successful experimental design and execution of the flow visualization portion of this research. Without these people, this research would not have been possible.

## References

- [1] John D. Anderson. *Fundamentals of Aerodynamics*. 5th. McGraw-Hill, 2011. ISBN: 9780073398105.
- [2] ATI Industrial Automation. "F/T sensor nano17". In: URL: [https://www.ati-ia.com/products/ft/ft\\_models.aspx?id=nano17](https://www.ati-ia.com/products/ft/ft_models.aspx?id=nano17).
- [3] S. Brousmiche et al. "Modeling of Wake-Vortex Detection by a Ground-based Fiber LIDAR System". In: Oct. 2009. ISBN: 978-953-307-005-6. doi: 10.5772/8325.
- [4] Nelson Andrew Brown. "Wake Surfing: Automated Cooperative Trajectories". In: 2017.
- [5] Chang-Koon Choi and Dae-Kun Kwon. "Wind tunnel blockage effects on aerodynamic behavior of bluff body". In: *Wind Struct Int J* 1.4 (1998), pp. 351–364.
- [6] Brian Dunbar. "About Aeronautics Research Mission Directorate". In: (2022). URL: <https://www.nasa.gov/aeroresearch/about-armd>.
- [7] Curtis Hanson et al. "Experimental Measurements of Fuel Savings During Aircraft Wake Surfing". In: June 2018. doi: 10.2514/6.2018-3560.
- [8] Harry Ku. *Notes on the Use of Propagation of Error Formulas*. Vol. 70C. 4. Journal of research of the national bureau of standards- C. Engineering and Instrumentation, 1966, pp. 263–273.
- [9] Warren Phillips and Douglas Hunsaker. "Lifting-Line Predictions for Induced Drag and Lift in Ground Effect". In: vol. 50. June 2013. doi: 10.2514/6.2013-2917.
- [10] Pasquale Sforza. "Chapter 9 - Drag Estimation". In: *Commercial Airplane Design Principles*. Ed. by Pasquale Sforza. Boston: Butterworth-Heinemann, 2014, pp. 349–404. ISBN: 978-0-12-419953-8. doi: <https://doi.org/10.1016/B978-0-12-419953-8.00009-7>. URL: <https://www.sciencedirect.com/science/article/pii/B9780124199538000097>.
- [11] H. Shen et al. "ENERGY-SAVING FORMATION FLIGHT: A REVIEW OF THE PAST, PRESENT, AND FUTURE". In: *International Journal of Innovative Research in Technology Science(IJIRTS)* 4.3 (2016). ISSN: 2321-1156.
- [12] H. Weimerskirch, J. Martin, and Y. et al Clerquin. "Energy saving in flight formation". In: *Nature* (2001), pp. 697–698. doi: 10.1038/35099670.
- [13] G. S. West and C. J. Apelt. "The effects of tunnel blockage and aspect ratio on the mean flow past a circular cylinder with Reynolds numbers between 104 and 105". In: *Journal of Fluid Mechanics* 114 (1982), pp. 361–377. doi: 10.1017/S0022112082000202.